# The stabilizing effect of high pore-fluid pressure along subduction megathrust faults: Evidence from friction experiments on accretionary sediments from the Nankai Trough

John D. Bedford[1,2], Daniel R. Faulkner[1], Michael J. Allen[1] and Takehiro Hirose[2]

[1]Rock Deformation Laboratory, Department of Earth, Ocean and Ecological Sciences, University of Liverpool, Liverpool, L69 3GP, UK

[2]Kochi Institute for Core Sample Research (X-star), Japan Agency for Marine-Earth Science and Technology (JAMSTEC), 200 Monobe-otsu, Nankoku, Kochi 783-8502, Japan

Corresponding author: John Bedford (jbedford@liverpool.ac.uk)

## Highlights

- Nankai accretionary sediments exhibit strong rate-strengthening friction behaviour
- Frictional stability increases at high pore-fluid pressure: more rate-strengthening
- Effective normal stress at constant pore pressure has minimal effect on stability
- Elevated pore-fluid pressure may promote slow- or aseismic slip in subduction zones

**Abstract**

Pore-fluid pressure is an important parameter in controlling fault mechanics as it lowers the effective normal stress, allowing fault slip at lower shear stress. It is also thought to influence the nature of fault slip, particularly in subduction zones where areas of slow slip have been linked to regions of elevated pore-fluid pressure. Despite the importance of pore-fluid pressure on fault mechanics, its role on controlling fault stability, which is determined by the friction rate parameter $(a - b)$, is poorly constrained, particularly for fault materials from subduction zones. In the winter of 2018-19 the accretionary complex overlying Nankai Trough subduction zone (SW Japan) was drilled as part of Integrated Ocean Drilling Program (IODP) Expedition 358. Here we test the frictional stability of the accretionary sediments recovered during the expedition by performing a series of velocity-stepping experiments on powdered samples (to simulate fault gouge) while systematically varying the pore-fluid pressure and effective normal stress conditions. The Nankai gouges, despite only containing 25% phyllosilicates, are strongly rate-strengthening and exhibit negative values for the rate-and-state parameter $b$. We find that for experiments where the effective normal stress is held constant and the pore-fluid pressure is increased the Nankai gouges become more rate-strengthening, and thus more stable. In contrast, when the pore-fluid pressure is held constant and the effective normal stress is varied, there is minimal effect on the frictional stability of the gouge. The increase in frictional stability of the gouge at elevated pore-fluid pressure is caused by an evolution in the rate-and-state parameter $b$, which becomes more negative at high pore-fluid pressure. These results have important implications for understanding the nature of slip in subduction zones and suggest the stabilizing effect of pore-fluid pressure could promote slow slip or aseismic creep on areas of the subduction interface that might otherwise experience earthquake rupture.

## 1. Introduction

Seismicity in subduction zones can result in megathrust earthquakes, the largest earthquakes in the world, often generating devastating tsunamis which pose a significant threat to human life and infrastructure in nearby coastal communities. Understanding the nature of the systems that produce

these earthquakes, and the fault zones from which they arise, is therefore paramount in the mitigation of damage and loss of human life in future events. The Nankai Trough subduction zone lies off the coast of southwest Japan, with records of creep, slow-slip events and megathrust earthquakes occurring on the fault dating back over 1000 years (Ando, 1975). In the winter of 2018-19 the accretionary complex that overlies the Nankai megathrust was drilled, with cuttings and core samples collected, to a maximum depth of 3262.5 mbsf (meters below seafloor) at Integrated Ocean Discovery Program (IODP) Site C0002 during Expedition 358 (Tobin et al., 2020), as part of the Nankai Trough Seismogenic Zone Experiment (NanTroSEIZE) (Tobin and Kinoshita, 2006). Here we experimentally test the frictional properties of the materials recovered during Expedition 358. We investigate how the frictional stability, which is determined by the rate-and-state parameter ($a - b$), varies over a range of pore-fluid pressure and effective normal stress conditions, which are representative of realistic in situ stresses found along the main subduction megathrust fault at seismogenic depths. Understanding the dependence of ($a - b$) on pore-fluid pressure and effective normal stress is important for elucidating how different modes of fault slip, whether it be aseismic creep, slow-slip or earthquake rupture, may occur along the subduction interface.

### *1.1. Geological setting of the Nankai Trough and experimental samples*

The Nankai Trough is located off the coast of southwest Japan (Fig. 1), where the Philippine Sea plate is subducted beneath the Eurasian plate at a rate of ~4-6 cm/yr (Seno et al., 1993). There is a long documented history of great earthquakes (with moment magnitude Mw >8) along the Nankai Trough, with recurrence intervals of ~90-150 years, and events often occurring in pairs, the most recent of which are the 1944 Tonankai (Mw 8.1) and the 1946 Nankaido (Mw 8.3) earthquakes (Ando, 1975). The 1944 event also produced a large tsunami, leading to widespread damage and loss of life along coastal areas of southwest Japan, that is thought to have been generated by earthquake rupture along a steeply-dipping splay fault branching up from the main subduction interface and cutting through the overlying accretionary prism (Park et al., 2002). As well as tsunamigenic earthquakes, a range of other fault slip behaviours have been observed in the Nankai Trough, including slow-slip events (Araki et al., 2017;

Kodaira et al., 2004) and very low-frequency earthquakes (Ito and Obara, 2006; Sugioka et al., 2012), highlighting the variety of fault slip modes that occur in subduction zones.

The Nankai accretionary prism, which overlies the main subduction interface, consists of hemipelagic sediments that have been scraped off the subducting Philippine plate, and can be divided into the inner and outer wedges (Fig. 1b) which are separated by megasplay faults (Kimura et al., 2007). Previous NanTroSEIZE expeditions have drilled across the accretionary prism at various localities including the frontal thrust, the megasplay fault and into the overlying Kumano forearc basin (e.g. Kinoshita et al., 2009). Site C0002 is located in the inner accretionary prism above the main megathrust at a depth of ~5200 mbsf (Fig. 1b). This site was first drilled as part of IODP Expeditions 326, 338 and 348, and extended during Expedition 358 to a depth of 3262.5 mbsf (Kitajima et al., 2020). The samples used for experiments in this study are from drill cuttings recovered during this most recent extension of C0002, from a depth interval of 3212.5-3217.5 mbsf. At this depth the accretionary sediments primarily consist of silty claystone with minor amounts of fine-grained sandstone, siltstone and fine silty-claystone (Kitajima et al., 2020). Only cuttings from this depth interval were used in this study as we intend to investigate the role of varying pore-fluid pressure and effective normal stress on frictional stability, therefore we want to minimise the effects of any sample variability that might occur by using samples recovered from different depth intervals. Although it should be noted that these lithologies are typical of those found throughout the accretionary wedge system (Tobin et al., 2020) and we expect similar lithologies to be present along the main megathrust at seismogenic depths.

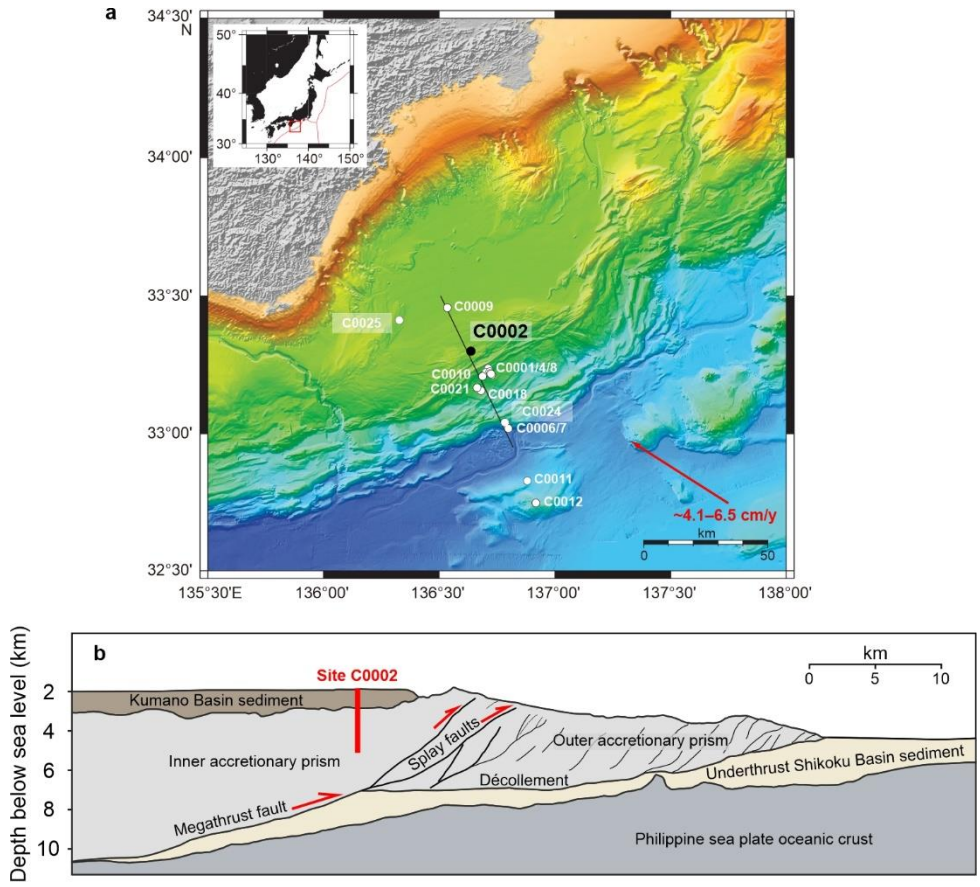


***Figure 1**: **a)** Bathymetric map of the Nankai Trough (modified from Tobin et al., (2020)) showing the NanTroSEIZE transect and drill sites of previous expeditions (white dots). The location of Site C0002 is shown as a black dot. **b)** Interpreted cross-section of the NanTroSEIZE transect (modified from Tobin et al., (2020)) showing Site C0002 which penetrated through the Kumano Basin and into the inner accretionary prism above the plate boundary megathrust fault.*

### *1.2. The roles of effective normal stress and pore-fluid pressure on fault stability*

The roles of effective normal stress and pore-fluid pressure on fault friction are typically considered together using the effective stress law ($\overline{\sigma_n} = \sigma_n - \alpha P_f$), where the effective normal stress ($\overline{\sigma_n}$) is equal to the normal stress ($\sigma_n$) minus the pore-fluid pressure ($P_f$) multiplied by the effective pressure coefficient ($\alpha$). For most brittle materials it is typically considered that $\alpha \approx 1$ (Terzaghi, 1943), meaning that changes in either the pore-fluid pressure or the normal stress will have an equal effect on friction. As the friction coefficient ($\mu$), the ratio of shear stress ($\tau$) to effective normal stress ($\mu = \tau/\overline{\sigma_n}$), of most

geological materials is relatively constant over a wide range of effective normal stresses (Byerlee, 1978), any increase in pore-fluid pressure will thus allow fault slip to occur at lower shear stress. However, this does not dictate whether seismic (unstable) or aseismic (stable) slip will occur. Instead, the stability of fault slip is thought to be controlled by the rate-dependence of slip, derived from the rate-and-state constitutive relations for frictional sliding (e.g. Dieterich, 1979; Marone, 1998; Scholz, 1998). The rate-dependence of slip is described by the friction parameter $(a - b)$:

$$(a - b) = \Delta\mu_{ss}/\Delta lnV$$

where $\mu_{ss}$ is the steady-state friction coefficient and $V$ is the sliding velocity. When $(a - b)$ is positive then the sliding behaviour is rate-strengthening ($\mu_{ss}$ increases as $V$ increases) and stable slip will prevail. In contrast, negative values of $(a - b)$ are associated with rate-weakening behaviour and are a prerequisite for unstable slip.

There have been several previous experimental investigations into the rate-dependence of different fault materials, where either the effective normal stress and/or pore-fluid pressure have been varied. Although distinguishing the roles of $\overline{\sigma_n}$ and/or $P_f$ on the rate-dependence of slip is commonly not the primary aim of these previous investigations, we have collated $\overline{\sigma_n}$ and $P_f$ trends from these datasets in Table 1. We report the range of $\overline{\sigma_n}$ and $P_f$ test conditions for each study and the range of $(a - b)$ values recorded. We also note any relationships between $\overline{\sigma_n}$, $P_f$ and $(a - b)$, and whether they are positive (i.e. as $\overline{\sigma_n}$ or $P_f$ increase, $(a - b)$ increases) or negative (as $\overline{\sigma_n}$ or $P_f$ increase, $(a - b)$ decreases). Firstly if we consider the relationships between $\overline{\sigma_n}$ and $(a - b)$, some gouges from natural fault zones show a positive relationship (e.g. Kurzawski et al., 2018, 2016; Smith and Faulkner, 2010) whereas others show a negative relationship (e.g. Carpenter et al., 2015, 2012; Rabinowitz et al., 2018). This contrast is likely due to differences in the gouge compositions, highlighted further by studies on synthetic gouges where the composition is controlled. For example quartz gouges typically show a negative relationship between $\overline{\sigma_n}$ and $(a - b)$ (Mair and Marone, 1999; Marone et al., 1990), whereas carbonate (Scuderi et al., 2013; Scuderi and Collettini, 2016) and smectite gouges (Saffer et al., 2001; Saffer and Marone, 2003) often show positive relationships. It should be noted, however, that although smectite shows a

positive relationship between $\overline{\sigma_n}$ and $(a-b)$, many other phyllosilicate minerals show no relationship (Table 1).

Compared to studies investigating the role of $\overline{\sigma_n}$, there are relatively few where the role of $P_f$ alone on $(a-b)$ has been investigated. This requires experiments where $\overline{\sigma_n}$ is kept constant while $P_f$ is systematically varied. Experiments on the input sediments to the Middle America trench suggest that $P_f$ has a positive relationship with $(a-b)$ (Kurzawski et al., 2018, 2016). In contrast, fluid-injection experiments on calcite gouge suggest that $P_f$ has a negative relationship with $(a-b)$ (Scuderi and Collettini, 2016), although it is difficult to separate the roles of $P_f$ and $\overline{\sigma_n}$ in these studies. Other variables have also been shown to influence the rate-dependence of friction including temperature (Okamoto et al., 2020; Sawai et al., 2016), sliding velocity (Carpenter et al., 2016; Ikari et al., 2009a; Saffer and Marone, 2003) and gouge composition (den Hartog and Spiers, 2013), demonstrating that care must be taken when interpreting rate-and-state data from experiments where multiple parameters have been varied. Xing et al., (2019) independently investigated the role of $P_f$ on the frictional stability of quartz, olivine, antigorite and chrysotile gouges and found a positive relationship between $P_f$ and $(a-b)$, with antigorite exhibiting the strongest positive relationship, which they explain by a dilatant hardening mechanism in the gouge. In this study we aim to test if the relationships observed by Xing et al., (2019) also occur in clay-rich materials collected from a subduction zone, where variable pore-fluid pressure is often invoked to explain the wide range of slip behaviour observed in these tectonic settings (e.g. Kodaira et al., 2004; Warren-Smith et al., 2019).

| Material | Study | $\overline{\sigma_n}$ (MPa) | $P_f$ (MPa) | $(a-b)$ | $(a-b)$ relationship with $\overline{\sigma_n}$ | $(a-b)$ relationship with $P_f$ | Notes |
|---|---|---|---|---|---|---|---|
| *Natural fault gouges:* | | | | | | | |
| Hikurangi Trench (New Zealand) | **[1]** | 1-150 | 0.5-15 | -0.0028 to 0.021 | Negative | Not reported | Calcareous mudstone input sediments |
| Middle America Trench (Co. Rica) | **[2,3]** | 30-110 | 20-120 | -0.015 to 0.023 | Positive | Positive | Silty clay gouge |
| Panamint Valley Normal Fault (USA) | **[4]** | 5-150 | Dry (RH) | 0.002 to 0.010 | None | - | Quartz-feldspar-calcite-clay mixtures |
| San Andreas Fault (USA). | **[5,6]** | 7-100 | 3-20 | 0.004 to 0.019 | Negative | Not reported | CDZ (Saponite clay-quartz mixtures) |
| Zuccale Normal Fault (Italy) | **[7]** | 20-150 | 13-240 | -0.062 to 0.045 | Complex | Complex | (a-b) dependent on $\overline{\sigma_n}$, $P_f$, temp. and vel. |
| Zuccale Normal Fault (Italy) | **[8]** | 25-75 | 50 | -0.001 to 0.007 | Positive | - | Variable composition fault gouges |
| *Quartz gouges:* | | | | | | | |
| Quartz | **[9]** | 25-75 | Dry (RH) | -0.007 to 0.014 | Neg. (weak) | - | Neg. at disp. >5 mm |
| Quartz | **[10]** | 50-190 | 5 or 10 | 0.0017 to 0.0044 | Negative | - | |
| Quartz | **[11]** | 70 | 5-60 | 0.0025 to 0.0043 | - | Positive (weak) | |
| *Phyllosilicate-rich gouges:* | | | | | | | |
| Chlorite | **[12]** | 100-400 | 50-220 | -0.009 to 0.016 | None | None | Temp = 22-600°C |
| Chlorite | **[13]** | 12-58 | 5 | 0.003 to 0.010 | None | - | (a-b) is vel dependent |
| Illite | **[13]** | 12-58 | 5 | 0.003 to 0.010 | None | - | (a-b) is vel dependent |
| Illite | **[14]** | 5-150 | Dry (RH) | 0.0015 to 0.0040 | None | - | (a-b) is vel dependent |
| Illite-quartz | **[15]** | 25-200 | 50-200 | -0.023 to 0.037 | Negative | Positive (weak) | Qtz-fract. dependent |
| Montmorillonite | **[13]** | 12-58 | 5 | 0.001 to 0.006 | None | - | (a-b) is vel dependent |
| Montmorillonite | **[16]** | 10-70 | 10 | -0.0017 to 0.0040 | Negative | - | Temp = 25-150°C |
| Montmorillonite | **[17]** | 10-700 | Dry or 10 | 0.0002 to 0.009 | Complex | - | |
| Smectite | **[14]** | 5-150 | Dry (RH) | -0.0030 to 0.0053 | Positive | - | (a-b) is vel dependent |
| Smectite | **[18]** | 5-50 | Dry (RH) | -0.0025 to 0.0053 | Positive | - | |
| *Carbonate/evaporite gouges:* | | | | | | | |
| Anhydrite-dolomite | **[19]** | 10-150 | Dry or 2 | -0.0020 to 0.0039 | Positive (weak) | - | |
| Calcite | **[20]** | 1-100 | Saturated | -0.005 to 0.013 | None | - | (a-b) is vel dependent |
| Calcite | **[21]** | 19-30 | 0-28 | 0 to 0.005 | Positive | Negative | Fluid injection exps. |
| Talc-calcite | **[22]** | 5-50 | Saturated | 0.0042 to 0.0107 | None | - | |
| *Other gouges:* | | | | | | | |
| Actinolite-chlorite | **[23]** | 50-200 | 50-200 | -0.018 to 0.052 | Positive (weak) | Positive (weak) | Temp. dependent |
| Antigorite | **[11]** | 30 or 70 | 5-90 | -0.0044 to 0.0094 | - | Positive | |
| Blueschist | **[24]** | 25-200 | 25-200 | -0.03 to 0.03 | Positive | - | $\overline{\sigma_n}/P_f = 0.5$ |
| Brucite | **[25]** | 10-60 | Saturated | -0.0047 to 0.0012 | Positive | - | |
| Chrysotile | **[11]** | 70 | 5-60 | 0.0047 to 0.0072 | - | Positive (weak) | |
| Olivine | **[11]** | 70 | 5-60 | 0.0050 to 0.0064 | - | Positive (weak) | |

***Table 1****: Collation of previous data on different fault gouges where (a-b) has been measured as effective normal stress and/or pore-fluid pressure is varied. RH = room/ambient humidity. The reference studies listed are:* ***[1]*** *Rabinowitz et al., (2018),* ***[2,3]*** *Kurzawski et al., (2018, 2016),* ***[4]*** *Numelin et al., (2007),* ***[5,6]*** *Carpenter et al., (2015, 2012),* ***[7]*** *Niemeijer and Collettini (2014),* ***[8]*** *Smith and Faulkner (2010),* ***[9]*** *Mair and Marone (1999),* ***[10]*** *Marone et al., (1990),* ***[11]*** *Xing et al., (2019),* ***[12]*** *Okamoto et al., (2019),* ***[13]*** *Ikari et al., (2009a),* ***[14]*** *Saffer and Marone (2003),* ***[15]*** *den Hartog and Spiers (2013),*

157 ***[16]*** *Mizutani et al., (2017)* ***[17]*** *Morrow et al., (2017),* ***[18]*** *Saffer et al., (2001),* ***[19]*** *Scuderi et al.,*
158 *(2013),* ***[20]*** *Carpenter et al., (2016),* ***[21]*** *Scuderi and Collettini (2016),* ***[22]*** *Giorgetti et al., (2015),*
159 ***[23]*** *Okamoto et al., (2020),* ***[24]*** *Sawai et al., (2016),* ***[25]*** *Okuda et al., (2021).*

160

161 *1.3. Previous investigations into the frictional behaviour of Nankai sediments*

162 To investigate the roles of effective normal stress and pore-fluid pressure on $(a - b)$ we use samples
163 collected from drilling of the Nankai Trough. Previous experimental studies on the frictional behaviour
164 of materials collected from Nankai drilling have been performed at low effective normal stresses (≤25
165 MPa) and pore-fluid pressures (≤5 MPa). These studies have shown that at slow sliding velocities (0.03-
166 100 $\mu m \cdot s^{-1}$) Nankai accretionary materials exhibit predominantly rate-strengthening behaviour (Ikari et
167 al., 2009b; Ikari and Saffer, 2011), in agreement with other studies on clay-rich gouge materials (e.g.
168 Ikari et al., 2009a; Morrow et al., 2017). However rate-weakening behaviour has been reported for
169 Nankai materials during experiments at low effective normal stress (5 MPa) (Tsutsumi et al., 2011), at
170 ultra-low, plate-rate velocities (Ikari and Kopf, 2017), and for intact samples that have high cohesive
171 strength (Roesner et al., 2020). Extreme dynamic weakening has also been observed in Nankai materials
172 during experiments approaching seismic slip rates (1.3 $ms^{-1}$) as a result of thermally-activated
173 weakening processes (Ujiie and Tsutsumi, 2010).

174 In this study we extend the range of previously investigated stress conditions on Nankai materials
175 by conducting frictional sliding experiments at effective normal stresses of 10-75 MPa and pore-fluid
176 pressures of 5-75 MPa, representative of in situ conditions that occur on the main megathrust fault in
177 nature. We test the effective stress law on the rate-dependence of slip by performing sets of velocity-
178 stepping experiments to measure $(a - b)$ where either the effective normal stresses or pore-fluid
179 pressure is held constant as the other is varied (summarized in Table 2).

180

## 2. Methods

### *2.1. Sample preparation*

Drill cuttings recovered from a depth interval of 3212.5-3217.5 mbsf were used for experiments. First, the cuttings were washed to remove any residue drilling mud before being left to dry in an oven at 60°C for 24 hours. Cuttings were then crushed and sieved to form a simulated gouge powder with a grain size of <125 μm, similar to sample preparation methodologies used in previous studies (e.g. Carpenter et al., 2015; Kurzawski et al., 2018; Rabinowitz et al., 2018).

X-ray Diffraction (XRD) analysis was used to determine the mineralogical composition of the simulated gouge. Representative sub-samples were crushed, in distilled water, to a powder <10 μm using an agate McCrone micronizing mill, and dried at 60°C. Dried samples were then crushed into a light and loose powder in an agate pestle and mortar before being back-loaded into a cavity holder as random powders. A copper X-ray tube was used, with a nickel filter to select for copper K-α radiation. Scans covered the range of 4-70° 2θ. To determine the presence of swelling clay (smectite) the powdered samples were saturated with ethylene glycol, by the vapour pressure method at 60 °C for 24 h and rescanned. Quantification of the mineralogy was achieved using the Relative Intensity Ratio (RIR) method (Hillier, 2000). XRD results showed the Nankai gouge to be comprised of quartz (49%), plagioclase (21%), illite (14%), K-feldspar (6%), chlorite (5%) and smectite (5%).

### *2.2. Experimental procedure*

Gouge layers are sheared at ambient temperature in a direct-shear geometry (Fig. 2) within a conventional triaxial deformation apparatus (see Faulkner and Armitage, 2013). The gouge is measured by weight to produce a layer with an initial thickness of ~1 mm that is placed between direct-shear forcing blocks (e.g. Sánchez-Roa et al., 2017). Soft silicone spacers are positioned at each end to allow shear of the layer to be accommodated without supporting any load. Grooves (200 μm deep, with a 400 μm spacing) are cut into the sliding area (50 x 20 mm) on the forcing blocks, perpendicular to the shear direction, to ensure that shear occurs within the layer itself and not between the edges of the gouge and

the forcing blocks. Once the layer is prepared the direct-shear assembly is wrapped in a low-friction PTFE sleeve (0.25 mm thickness) before being inserted into a 3 mm thick PVC jacket. The PTFE sleeve is used to minimize friction between the jacket and the direct-shear assembly in the vicinity of the layer. The jacketed direct-shear assembly is then positioned between the platens of the sample assembly and inserted into the pressure vessel of the triaxial apparatus. Normal stress is applied to the layer by the confining pressure, and pore-fluid pressure is introduced via three porous disks on each forcing block, spaced to ensure an even distribution of fluid (Fig. 2). Deionized water was used as the pore fluid in this study. Both the confining and pore-fluid pressures are held constant during an experiment by servo-controlled pumps attached to each pressure system, with a resolution of better than 0.05 MPa. The gouge layer is sheared by the axial piston and the applied force is measured via an internal force gauge with a measurement resolution of better than 0.05 kN. In this setup a maximum load-point displacement of 8.5 mm can be achieved, which equates to a shear strain ($\gamma$) of ~10, given the final layer thickness of ~0.85 mm.

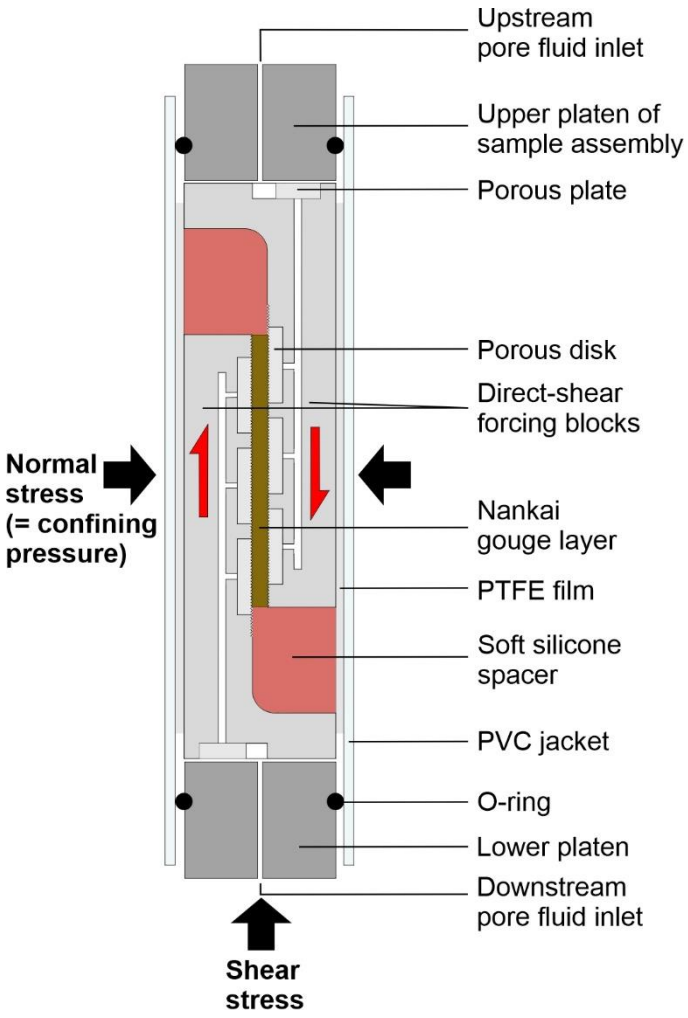


***Figure 2**: An illustration of the direct-shear experimental set up (piston diameter is 20 mm). The assembly is placed into a triaxial deformation apparatus where the confining pressure applies the normal stress across the gouge layer. Pore-fluid pressure is servo-controlled at the boundaries of the layer through three sintered stainless steel porous disks on each direct-shear forcing block.*

Experiments were performed over a total of 20 different stress-conditions (Table 2), at four different effective normal stresses (10, 25, 50 and 75 MPa) and five different pore-fluid pressures (5, 10, 25, 50 and 75 MPa). For example, for an experiment performed at 75 MPa effective normal stress and 75 MPa pore-fluid pressure, the confining pressure ($P_c$) is 150 MPa ($\overline{\sigma_n} = P_c - P_f$). In each experiment the gouge layers were sheared for an initial 1.5 mm displacement at 0.3 µm·s$^{-1}$, before velocity steps of 0.3 to 3 µm·s$^{-1}$ and back were applied every subsequent 1 mm of displacement to determine the rate-

dependence of slip, $(a - b)$. Data were acquired at a logging frequency of 10 Hz for all tests in this study. The rate-and-state parameters, $a$ and $b$, were determined by processing the velocity steps using the RSFit3000 program (Skarbek and Savage, 2019) which applies an inverse modelling technique with an iterative least-squares fit. The program also solves for $D_c$ (reported in Supplementary Tables 1 and 2) and treats the stiffness as a fitting parameter.

At the end of each experiment the permeability of the gouge was measured using the transient pulse decay method (see Brace et al., 1968). This involves abruptly increasing $P_f$ by approximately 0.5 MPa at the upstream end of the sample, producing a pressure differential across the gouge layer. This pressure differential then decays with time as the pore-fluid dissipates through the sample allowing for the permeability to be calculated.

| **Experiment** | $\overline{\sigma_n}$ **(MPa)** | $P_f$ **(MPa)** | $P_c$ **(MPa)** | **Velocity (μm·s$^{-1}$)** |
|---|---|---|---|---|
| Nankai 1 | 10 | 5 | 15 | 0.3 - 3 |
| Nankai 2 | 10 | 10 | 20 | 0.3 - 3 |
| Nankai 3 | 10 | 25 | 35 | 0.3 - 3 |
| Nankai 4 | 10 | 50 | 60 | 0.3 - 3 |
| Nankai 5 | 10 | 75 | 85 | 0.3 - 3 |
| Nankai 6 | 25 | 5 | 30 | 0.3 - 3 |
| Nankai 7 | 25 | 10 | 35 | 0.3 - 3 |
| Nankai 8 | 25 | 25 | 50 | 0.3 - 3 |
| Nankai 9 | 25 | 50 | 75 | 0.3 - 3 |
| Nankai 10 | 25 | 75 | 100 | 0.3 - 3 |
| Nankai 11 | 50 | 5 | 55 | 0.3 - 3 |
| Nankai 12 | 50 | 10 | 60 | 0.3 - 3 |
| Nankai 13 | 50 | 25 | 75 | 0.3 - 3 |
| Nankai 14 | 50 | 50 | 100 | 0.3 - 3 |
| Nankai 15 | 50 | 75 | 125 | 0.3 - 3 |
| Nankai 16 | 75 | 5 | 80 | 0.3 - 3 |
| Nankai 17 | 75 | 10 | 85 | 0.3 - 3 |
| Nankai 18 | 75 | 25 | 100 | 0.3 - 3 |
| Nankai 19 | 75 | 50 | 125 | 0.3 - 3 |
| Nankai 20 | 75 | 75 | 150 | 0.3 - 3 |

***Table 2****: Summary of experiments performed in this study.*

## 3. Results

### *3.1. Frictional strength and behaviour*

An example of a typical frictional sliding test is shown in Figure 3a. The gouge samples initially undergo quasi-elastic loading, shown by the steep increase in coefficient of friction, before yielding and the initiation of steady-state sliding at approximately 1 mm of load point displacement. The friction coefficient of the Nankai gouge at steady-state sliding is between 0.37-0.45 for all tests, with negligible cohesion (Fig. 3c). Note that the reported shear stress values in Figure 3c were taken at 1.5 mm displacement, after the initiation of steady-state slide and before the first velocity step in each test. The range of strength values is likely a result of sample variability as the coefficient of friction is independent of the effective normal stress and pore-fluid pressure conditions (Fig. 3c). This suggests that the mechanical (frictional) strength obeys the effective stress law ($\overline{\sigma_n} = \sigma_n - \alpha P_f$) and the effective pressure coefficient ($\alpha$) for this parameter is approximately equal to 1.

The Nankai gouge exhibits strongly rate-strengthening frictional behaviour, with ($a - b$) ranging from 0.0042 to 0.0219 across all tests in this study as $\overline{\sigma_n}$ and $P_f$ are varied. The majority of the velocity steps are characterised by negative b-values (Fig. 3b), which have been widely observed for other phyllosilicate-rich gouges (Carpenter et al., 2015; Ikari et al., 2009a; Sánchez-Roa et al., 2017; Scuderi and Collettini, 2018; Smith and Faulkner, 2010). The Nankai gouge also exhibits an asymmetrical frictional response to up-steps and down-steps in the sliding velocity (Fig. 3b), with ($a - b$) values determined from down-steps in the sliding velocity (3 to 0.3 μm·s$^{-1}$) being greater (i.e. more rate-strengthening) than those determined from up-steps in the sliding velocity (0.3 to 3 μm·s$^{-1}$). Similar asymmetrical responses have been reported previously (Rathbun and Marone, 2013; Xing et al., 2019) and are hypothesised to be related to differences in the grain-scale response of granular gouges to velocity increases and decreases (Rathbun and Marone, 2013).

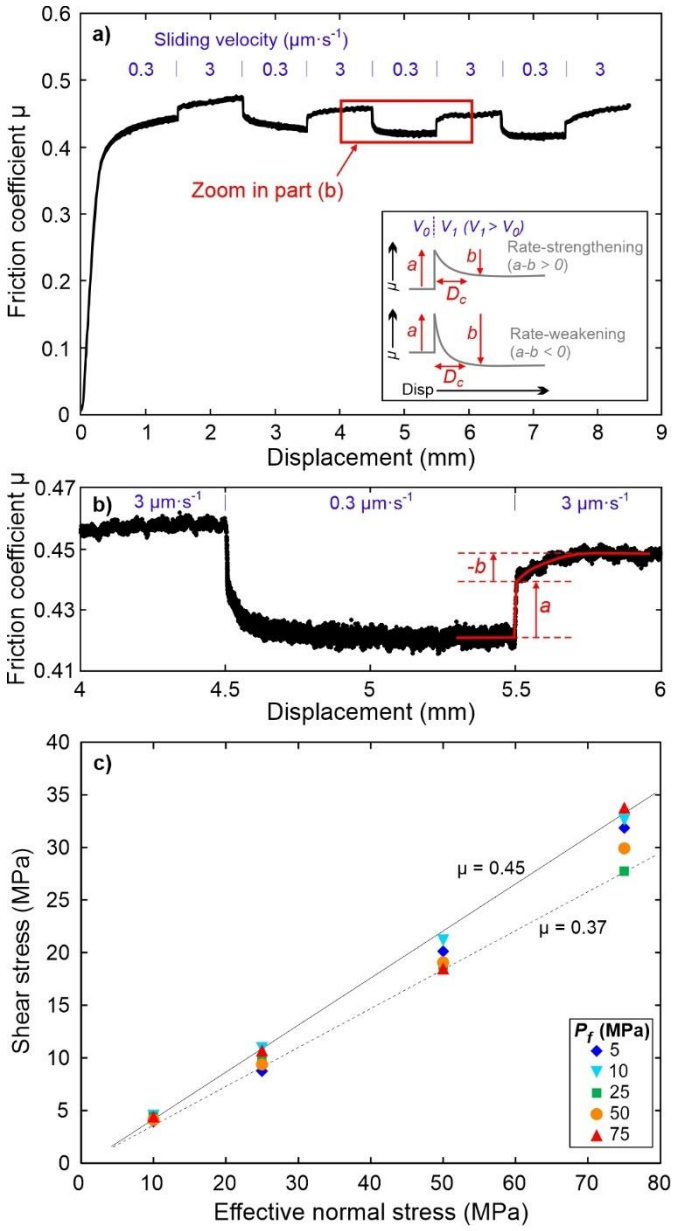


***Figure 3**: **a)** An example of a complete experiment ($\overline{\sigma_n}$ = 25 MPa, $P_f$ = 75 MPa) showing the evolution of the coefficient of friction with displacement as the sliding velocity is stepped between 0.3 and 3 μm·s$^{-1}$. The inset shows how the coefficient of friction typically evolves for rate-strengthening and rate-weakening materials, where the friction rate parameters a and b are both positive. **b)** A zoom on velocity steps from the experimental data on Nankai gouge shown by the box in (a) highlighting the rate-strengthening nature of the gouge and the occurrence of negative b-values. **c)** Shear stress as a function of normal stress for all tests in this study. The reported shear stress values are after 1.5 mm displacement (just before the first velocity step).*

278 *3.2. The roles of effective normal stress and pore-fluid pressure on the velocity dependence of*
279 *friction*

280 The $(a-b)$ values of the Nankai gouge are shown in Figure 4 as a function of (1) effective normal
281 stress at constant pore-fluid pressure, and (2) pore-fluid pressure at constant effective normal stress.
282 Note that only the $(a-b)$ values calculated from velocity up-steps (0.3 to 3 μm·s$^{-1}$) are shown, with
283 the average up-step values for a given test shown in bold and connected by contours of equal $\overline{\sigma_n}$ or $P_f$.
284 At constant pore-fluid pressure there is a decrease in $(a-b)$ between 10 and 25 MPa effective normal
285 stress, however when $\overline{\sigma_n} \geq 25$ MPa, the $(a-b)$ values are largely independent of effective normal stress
286 (Fig. 4a). In contrast, at constant effective normal stress there is a systematic increase in $(a-b)$ with
287 pore-fluid pressure, with the gouge become more rate-strengthening at elevated $P_f$ (Fig. 4b). Again,
288 there is a difference in the frictional behaviour between 10 and 25 MPa effective normal stress with no
289 clear pore-fluid pressure dependence for tests conducted at $\overline{\sigma_n}$ = 10 MPa.

290 The results collected at $\overline{\sigma_n}$ = 10 MPa exhibit greater scatter and do not show as clear a trend as the
291 tests when $\overline{\sigma_n} \geq 25$ MPa. Consequently, we have included this data with dashed lines so as to emphasise
292 the clear trends in the results of the data. We discuss the possible reasons for the behaviour at $\overline{\sigma_n} =10$
293 MPa later in the paper. It should also be noted that there is no obvious dependence of characteristic slip
294 weakening distance, $D_c$, with either $\overline{\sigma_n}$ or $P_f$. All of the rate-and-state parameters ($a$, $b$ and $D_c$) for each
295 velocity step are reported in Supplementary Tables 1 and 2.

296 As we have tested the rate-dependence of friction, $(a-b)$, of the Nankai gouge over a range of
297 pore-fluid pressure and normal stress conditions, the data can also be plotted as a pore-fluid factor, λ
298 (where $\lambda = P_f/\sigma_n$). Although there is a positive relationship between $(a-b)$ and λ (i.e. $(a-b)$
299 increases as λ increases), it is more difficult to separate the individual contributions of $P_f$ and $\overline{\sigma_n}$ when
300 the data are plotted in this way, therefore we have chosen to present this data in the supplementary
301 material (see Supplementary Figure 1). In contrast, the results in Fig. 4 clearly show that the main
302 control over $(a-b)$ is provided by $P_f$, with $\overline{\sigma_n}$ having minimal effect on the frictional stability of the
303 gouge.

The pore-pressure dependence on $(a-b)$ that we observe for tests conducted at $\overline{\sigma_n} \geq 25$ MPa on Nankai gouge is similar to that observed by Xing et al., (2019) for antigorite gouge. For example in our data, when $\overline{\sigma_n} = 75$ MPa, the average up-step $(a-b)$ value increases from 0.00645 at $P_f = 5$ MPa, to 0.01053 at $P_f = 75$ MPa. This corresponds to ~0.85% increase in $(a-b)$ per MPa of pore-fluid pressure, which is similar to the 1% increase in $(a-b)$ per MPa reported by Xing et al., (2019) for antigorite gouge.

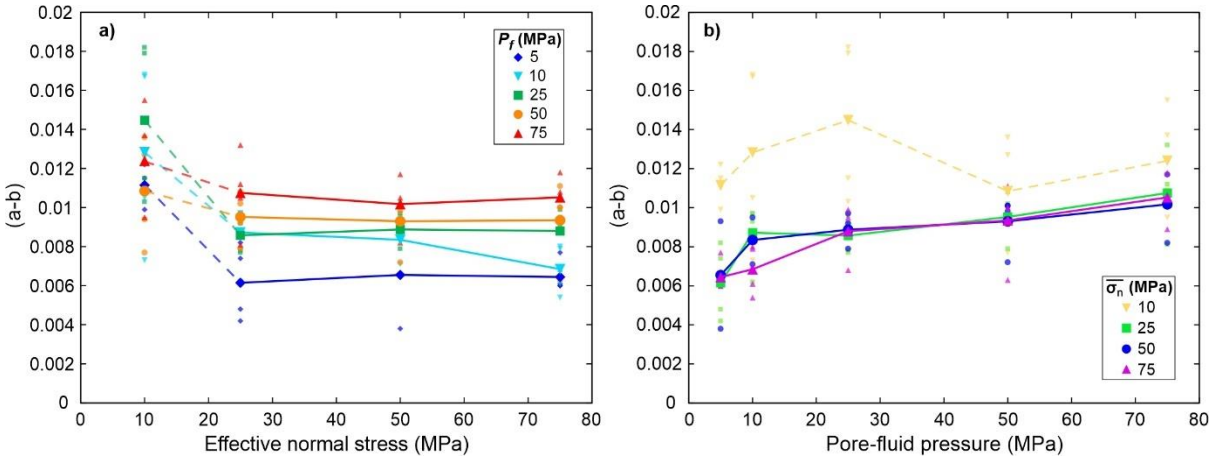


***Figure 4****: The rate-dependence of slip, $(a-b)$, plotted as a function of* ***a)*** *effective normal stress and* ***b)*** *pore-fluid pressure. Note only the $(a-b)$ values determined from the velocity up-steps (0.3 to 3 μm·s$^{-1}$) are shown. Small symbols are all the up-step $(a-b)$ data points calculated from every experiment in this study, with the average $(a-b)$ values for a given experiment shown in bold and connected by contours of constant $P_f$ or $\overline{\sigma_n}$. The contours are dashed between 10 and 25 MPa effective normal stress as there is a change in the frictional response between these points, with a strong $P_f$ dependence on $(a-b)$ at $\overline{\sigma_n} \geq 25$ MPa.*

To elucidate further the cause of the pore pressure dependence observed in Figure 4, the average up-step values for the individual friction rate parameters $a$ and $b$ are plotted in Figure 5. The friction rate parameter $a$ is always higher than $b$, leading to the rate-strengthening behaviour observed for Nankai gouge. The data show that the friction rate parameter $a$ is largely independent of the pore-fluid pressure (Fig. 5a), with values between 0.006-0.0076 for the entire range of pore-fluid pressures investigated. However, the friction rate parameter $b$ shows a negative dependence on pore-fluid pressure, decreasing from ~0 at $P_f = 5$ MPa, to -0.0032 at $P_f = 75$ MPa (Fig. 5b), highlighting that changes in $b$ with pore-fluid pressure are responsible for the increased frictional stability.

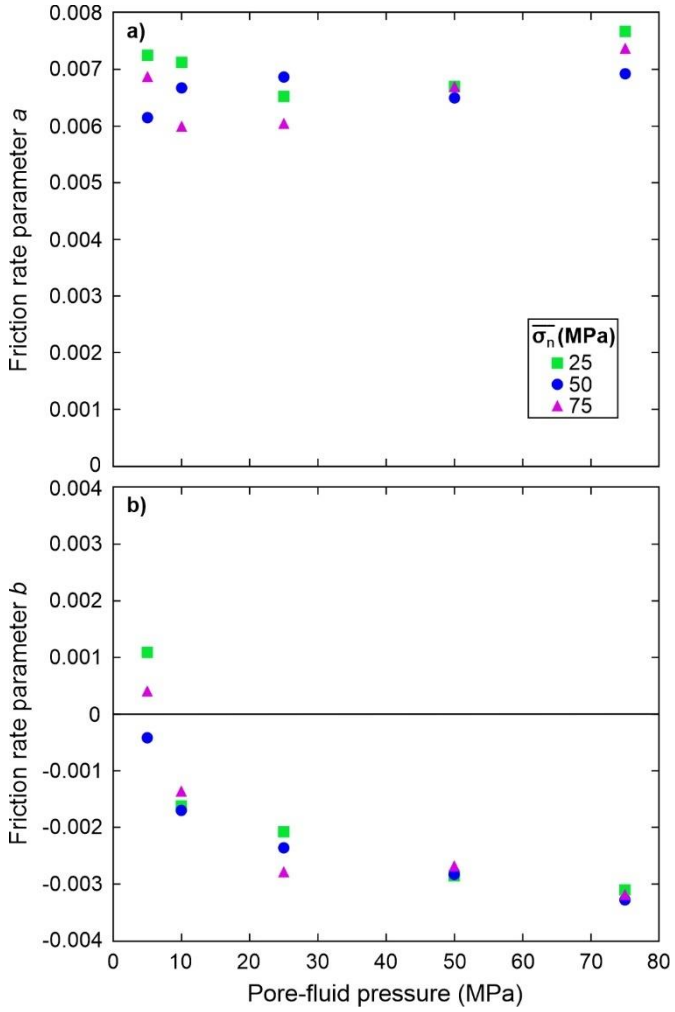


***Figure 5**: Evolution of **a)** the friction rate parameter a, and **b)** the friction rate parameter b as a function of pore-fluid pressure.*

### *3.3. Gouge permeability*

The permeability of the Nankai gouge measured at the end of each experiment is low, with values in the range of $10^{-21}$ to $10^{-22}$ $m^2$ (Fig. 6). The permeability is dependent on the effective normal stress, with the lowest values occurring at high $\overline{\sigma_n}$. There does not appear to be any pore-fluid pressure dependence on the measured permeability values (Fig. 6). The slow run-in rates at which the samples were initially displaced, coupled with the permeability of the gouge suggest that excess pore-fluid pressures did not develop within the gouge and adversely affect the experimental results presented (see Faulkner et al., 2018).

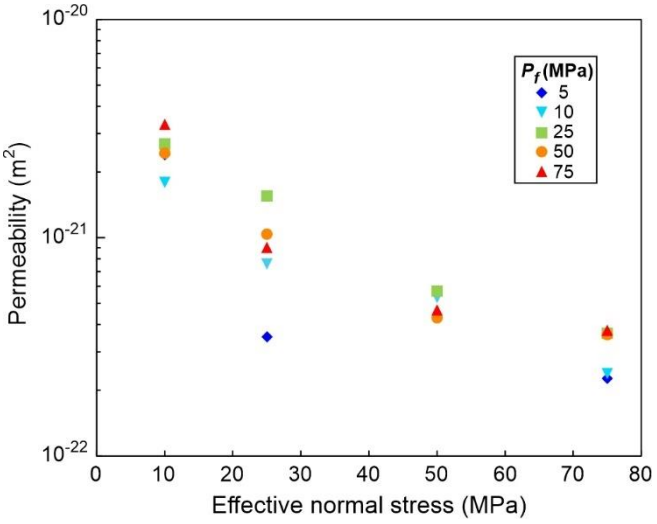


***Figure 6****: Permeability of the Nankai gouge measured at the end of each experiment plotted against effective normal stress. Gouge permeability decreases with increasing effective normal stress.*

## 4. Discussion

### *4.1. The stabilizing effect of pore-fluid pressure on frictional behaviour*

The Nankai gouge used in this study is rate-strengthening with $\mu \approx 0.4$, consistent with the majority of previous frictional investigations of fault materials collected from the Nankai Trough (Ikari et al., 2009b; Ikari and Saffer, 2011) and in good agreement with the frictional properties of other clay-rich

materials (e.g. Ikari et al., 2009a; Morrow et al., 2017). The results presented in Figure 4 show that under realistic in situ stresses the velocity dependence of Nankai accretionary materials is more sensitive to pore-fluid pressure than effective normal stress, with high $P_f$ leading to higher $(a-b)$ values. As the gouge becomes more rate-strengthening at elevated $P_f$, it can be concluded that pore-fluid pressure has a stabilizing effect on the gouge. This stabilizing effect has been similarly observed in the controlled $P_f$ tests of Xing et al., (2019) on quartz, olivine and serpentine gouges, as well as in studies on frictional behaviour of silty clay input sediments to the Middle America Trench, Costa Rica (Kurzawski et al., 2018), and on illite-quartz mixtures (den Hartog and Spiers, 2013).

The Nankai gouge exhibits a change in frictional stability between 10 and 25 MPa effective normal stress (Fig. 4), with the pore-pressure dependence of $(a-b)$ only observed for $\overline{\sigma_n} \geq 25$ MPa. Previous studies have shown that fault materials can exhibit different frictional behaviour at low normal stress, particularly phyllosilicate-rich gouges. For example, Behnsen and Faulkner (2012) observed a decrease in frictional strength of ten different phyllosilicate gouges as effective normal stress was increased from 5 to 20 MPa, above which the frictional strength remained almost constant. Similar behaviour has been observed in other studies on phyllosilicate-rich gouges (e.g. Ikari et al., 2007; Saffer and Marone, 2003), with Ikari et al., (2007) also observing a wide range of $(a-b)$ values at low normal stress. The transition we observe between 10 and 25 MPa effective normal stress is similar to change in frictional strength observed by Behnsen and Faulkner (2012) at 20 MPa. This could be caused by a different micromechanical response of the gouge at low effective normal stress, perhaps as a result of different compaction behaviour (Behnsen and Faulkner, 2012). Regardless of the cause of the switch in behaviour, the results clearly show that $(a-b)$ becomes independent of effective normal stress at $\overline{\sigma_n} \geq$ 25 MPa (Fig. 4a), with pore-fluid pressure exerting the dominant control on the frictional stability at these conditions (Fig. 4b).

The results in Figure 5 show that the increase in $(a-b)$ with $P_f$ is caused by a decrease the friction rate parameter $b$, which becomes more negative at elevated $P_f$ (Fig. 5b). The cause of negative $b$-values is still not fully understood but they have been widely reported in previous investigations on phyllosilicate-rich fault materials (e.g. Carpenter et al., 2015; Ikari et al., 2009a; Sánchez-Roa et al.,

2017; Scuderi and Collettini, 2018). Ikari et al., (2009a) suggest that in low permeability gouges the effect of dilational hardening immediately after a velocity step, where dilation reduces $P_f$ leading to a local increase in effective normal stress which strengthens the gouge, may explain the occurrence of negative $b$-values. However, if this was the case, the trend of the friction coefficient would actually reduce with time (and slip) as fluid pressure diffused back into the layer, thereby reducing the effective normal stress. Xing et al., (2019) also use dilational hardening as a mechanism to explain the increase in $(a-b)$ they observe with increasing $P_f$ in their study, although it should be noted that all of the $b$-values they report are positive or near zero. The permeability of the Nankai gouge in our study is sufficiently low (Fig. 6) that transient local pore-pressure perturbations after velocity steps may affect the bulk frictional response of the gouge (Faulkner et al., 2018), thus potentially explaining the negative $b$-values as hypothesised by Ikari et al., (2009a). However, the permeability of the gouge is predominantly controlled by $\overline{\sigma_n}$ not $P_f$ (Fig. 6). In contrast the negative $b$-values are largely independent of $\overline{\sigma_n}$ and are controlled by $P_f$ (Fig. 5b). This suggests that although transient pore-pressure variations may affect the frictional response of the gouge they cannot fully explain the cause of the negative $b$-values and why they become more negative with increasing $P_f$ in our experiments. This is further evidenced by previous experimental work where positive $b$-values have been reported for gouges with similarly low permeabilities to the Nankai gouge tested here (e.g. Morrow et al., 2017). Therefore the trends we observe in the velocity dependence of the Nankai gouge, where $(a-b)$ increases with $P_f$ as the $b$-values decrease, suggest that this is primarily caused by the inherent frictional properties of the gouge itself; any transient pore pressure effects that result from the low permeability nature of the gouge will likely only have a secondary effect on the bulk frictional behaviour (Ikari et al., 2009a).

The rate-parameter $b$ is often termed the evolution effect and is classically thought to represent a change in the asperity contact area after a velocity step (Dieterich and Kilgore, 1994; Marone, 1998). However, there has been debate in the literature as to whether the contact area hypothesis is the whole story, or whether the contact 'quality' (theory of adhesion; (Bowden and Tabor, 1950)) also affects the frictional properties. Another fundamental manifestation of the evolution effect is the time-dependent increase in frictional strength that occurs when rocks/gouge are held in stationary contact (often termed

403 "frictional aging"), which has also traditionally been attributed to an increase in contact area as a result
404 of asperity creep (Dieterich and Kilgore, 1994). In our study we observe mostly negative $b$-values,
405 which cannot easily be explained using the contact area argument (often colloquially referred to as the
406 "contact quantity" hypothesis). Negative b-values would imply that with slip, that contact area would
407 grow following a velocity step. Also, if the evolution of the rate-parameter $b$ were caused by an increase
408 in the real contact area then we would expect to see a dependence on effective normal stress, which we
409 do not observe (Fig. 5b). Instead we find that the rate-parameter $b$ is dependent on pore-fluid pressure
410 rather than effective normal stress. This observation may therefore support the main alternative
411 hypothesis to explain frictional aging; that it arises from time-dependent chemical bonding on the
412 frictional interface (e.g. Li et al., 2011; Thom et al., 2018), often referred to as the "contact quality"
413 hypothesis. Perhaps at elevated pore-fluid pressure the contact quality at asperities in the gouge is
414 enhanced, possibly as a result of structurally bound water layers on the surface of the gouge minerals
415 becoming more stable under these conditions (e.g. Israelachvili, 1992), causing the observed pore
416 pressure dependence on $b$.

417 Regardless of the cause of pore-pressure dependence on $(a - b)$, and the nature of the underlying
418 mechanism controlling the evolution of the rate-parameter $b$, it is clear that the gouge becomes more
419 rate-strengthening and thus more stable at high $P_f$. This is perhaps counterintuitive to the traditional
420 view on the role of $P_f$ on fault mechanics, where high $P_f$ is thought to lower $\overline{\sigma_n}$ and thus promote fault
421 slip at a lower shear stress. Our results show that besides the traditional mechanical effect of $P_f$, it also
422 has a direct influence on the velocity dependence of friction, $(a - b)$. Therefore elevated $P_f$ may
423 promote slip on a fault, but the nature of this slip is likely to be more stable than when $P_f$ is low,
424 potentially leading to slow-slip or aseismic creep.

425

426 *4.2. Implications for fault slip behaviour in subduction zones*

427 Subduction zones exhibit a variety of slip behaviour with depth, including aseismic creep, slow-
428 slip and stick-slip behaviour. It is widely considered that pore-fluid pressure exerts an important control

on fault slip behaviour in subduction zones, with elevated pore-fluid pressure often linked to areas of slow-slip (Kodaira et al., 2004; Warren-Smith et al., 2019). At the Nankai Trough it has also been hypothesised that stick-slip behaviour may be suppressed beneath the accretionary wedge by elevated pore-pressures maintaining a low effective normal stress (Tobin and Saffer, 2009). Our results support this hypothesis by demonstrating that elevated pore-fluid pressures actually increase the frictional stability of the fault materials themselves (Fig. 4), as well as maintain a low effective normal stress on the fault.

The wide array of fault slip behaviour that occurs in subduction zones is often attributed to heterogeneity in both material properties (Barnes et al., 2020; Kirkpatrick et al., 2020) and pore-fluid pressure (Hirose et al., in revision) along the subduction interface. Although the gouge material tested in this study exhibited exclusively rate-strengthening behaviour, previous investigations have shown that rate-weakening material can also be found within the Nankai Trough (e.g. Roesner et al., 2020), suggesting there is a heterogeneous distribution of material properties within the subduction zone. Based on the frictional stability, the material in the study would be expected to experience stable aseismic creep, whereas the material tested by Roesner et al., (2020) could experience unstable stick-slip behaviour, depending on the elastic stiffness of the surrounding materials (Leeman et al., 2016). Slow-slip often occurs in fault materials in the transitional region between stable and unstable slip (Bedford and Faulkner, 2021; Leeman et al., 2016), when the rate-dependence of friction, $(a - b)$, is close to zero. Along patches of the subduction zone interface where the material properties would otherwise be rate-weakening and promote unstable slip, we hypothesise that elevated pore-fluid pressures could shift these patches into a frictional stability regime where either slow-slip or aseismic creep would become more favourable. Our results therefore support the correlation between elevated pore-fluid pressures and the abundance of slow-slip observed in many subduction zones around the world (e.g. Behr and Bürgmann, 2021).

The materials tested in this study are clay-rich sediments that are typical of accretionary wedge materials found in the upper regions of subduction zones. At intermediate depths (50-200 km) in subduction zones seismic fault slip behaviour can also occur, even though at these depths it is typically

considered that the pressure is too high to allow brittle deformation to occur. It is thought that seismicity at intermediate depths is linked to the breakdown of hydrous minerals in the subducting slab, such as serpentine or lawsonite, and experiments performed under in situ conditions have supported the hypothesis that dehydration reactions can trigger seismic and slow slip at these depths (e.g. Okazaki and Hirth, 2016). Xing et al., (2019) tested the role of pore-fluid pressure on the frictional stability of serpentine and olivine gouges (i.e. materials linked to seismogenesis at intermediate depths in subduction zones) and found that elevated pore-fluid pressures also have a stabilizing effect on the frictional behaviour of these gouges, particularly for antigorite. This is a similar pore-fluid pressure dependence to what we observe for the clay-rich Nankai gouges in this study. Our results, alongside those of Xing et al., (2019), therefore suggest that pore-fluid pressure may stabilise faults across the entire seismogenic depth range of subduction zones.

## 5. Conclusions

Our results demonstrate that pore-fluid pressure has a stabilizing effect on Nankai accretionary materials, with $(a - b)$ increasing as $P_f$ is increased, whereas effective normal stress has minimal effect on the stability of the simulated fault gouge. The increase in $(a - b)$ at elevated $P_f$ is caused by an evolution in the rate-and-state parameter $b$ which becomes more negative at high $P_f$. These results have important implications for fault slip behaviour in subduction zones and suggest that regions of elevated pore-fluid pressure are more likely to experience slow-slip or aseismic creep than those where the pore-fluid pressure is low.

## Acknowledgments

This work used samples and shipboard data collected during Integrated Ocean Drilling Program (IODP) Expedition 358. We would like to thank the crew and the technicians (Marine Works Japan) of D/V Chikyu for their effort and support during the expedition**.** We thank Gary Coughlan for his

assistance in developing and maintaining the experimental equipment. We are also grateful to James Utley for help with XRD analysis. This work is supported by Natural Environment Research Council grants NE/S015531/1 and NE/P002943/1. The data reported in the figures can be accessed in National Geoscience Data Centre (NGDC) data repository: https://webapps.bgs.ac.uk/services/ngdc/accessions/index.html#item163985

## References

Ando, M., 1975. Source mechanisms and tectonic significance of historical earthquakes along the Nankai Trough, Japan. Tectonophysics 27, 119–140. https://doi.org/https://doi.org/10.1016/0040-1951(75)90102-X

Araki, E., Saffer, D.M., Kopf, A.J., Wallace, L.M., Kimura, T., Machida, Y., Ide, S., Davis, E., Scientists, I.E. 365 shipboard, 2017. Recurring and triggered slow-slip events near the trench at the Nankai Trough subduction megathrust. Science (80-. ). 356, 1157–1160. https://doi.org/10.1126/science.aan3120

Barnes, P.M., Wallace, L.M., Saffer, D.M., Bell, R.E., Underwood, M.B., Fagereng, A., Meneghini, F., Savage, H.M., Rabinowitz, H.S., Morgan, J.K., Kitajima, H., Kutterolf, S., Hashimoto, Y., Engelmann De Oliveira, C.H., Noda, A., Crundwell, M.P., Shepherd, C.L., Woodhouse, A.D., Harris, R.N., Wang, M., Henrys, S., Barker, D.H.N., Petronotis, K.E., Bourlange, S.M., Clennell, M.B., Cook, A.E., Dugan, B.E., Elger, J., Fulton, P.M., Gamboa, D., Greve, A., Han, S., Hupers, A., Ikari, M.J., Ito, Y., Kim, G.Y., Koge, H., Lee, H., Li, X., Luo, M., Malie, P.R., Moore, G.F., Mountjoy, J.J., McNamara, D.D., Paganoni, M., Screaton, E.J., Shankar, U., Shreedharan, S., Solomon, E.A., Wang, X., Wu, H.-Y., Pecher, I.A., LeVay, L.J., Scientists, I.E. 372, 2020. Slow slip source characterized by lithological and geometric heterogeneity. Sci. Adv. 6. https://doi.org/10.1126/sciadv.aay3314

506 Bedford, J.D., Faulkner, D.R., 2021. The role of grain size and effective normal stress on localization
507 and the frictional stability of simulated quartz gouge. Geophys. Res. Lett. 48, e2020GL092023.
508 https://doi.org/10.1029/2020gl092023

509 Behnsen, J., Faulkner, D.R., 2012. The effect of mineralogy and effective normal stress on frictional
510 strength of sheet silicates. J. Struct. Geol. 42, 49–61. https://doi.org/10.1016/j.jsg.2012.06.015

511 Behr, W.M., Bürgmann, R., 2021. What's down there? The structures, materials and environment of
512 deep-seated slow slip and tremor. Philos. Trans. R. Soc. A 379.
513 https://doi.org/10.1098/rsta.2020.0218

514 Bowden, F.P., Tabor, D., 1950. The friction and lubrication of solids, Part I. Clarendon Press, Oxford.

515 Brace, W.F., Walsh, J.B., Frangos, W.T., 1968. Permeability of granite under high pressure. J.
516 Geophys. Res. 73, 2225–2236. https://doi.org/10.1029/JB073i006p02225

517 Byerlee, J., 1978. Friction of Rocks. Pure Appl. Geophys. 116, 615–626.
518 https://doi.org/https://doi.org/10.1007/BF00876528

519 Carpenter, B.M., Collettini, C., Viti, C., Cavallo, A., 2016. The influence of normal stress and sliding
520 velocity on the frictional behaviour of calcite at room temperature: insights from laboratory
521 experiments and microstructural observations. Geophys. J. Int. 205, 548–561.
522 https://doi.org/10.1093/gji/ggw038

523 Carpenter, B.M., Saffer, D.M., Marone, C., 2015. Frictional properties of the active San Andreas
524 Fault at SAFOD: Implications for fault strength and slip behavior. J. Geophys. Res. Solid Earth
525 120, 5273–5289. https://doi.org/10.1002/2015JB011963

526 Carpenter, B.M., Saffer, D.M., Marone, C., 2012. Frictional properties and sliding stability of the San
527 Andreas fault from deep drill core. Geology 40, 759–762. https://doi.org/10.1130/G33007.1

528 den Hartog, S.A.M., Spiers, C.J., 2013. Influence of subduction zone conditions and gouge
529 composition on frictional slip stability of megathrust faults. Tectonophysics 600, 75–90.
530 https://doi.org/10.1016/j.tecto.2012.11.006

Dieterich, J.H., 1979. Modeling of rock friction 1. Experimental results and constitutive equations. J. Geophys. Res. 84, 2161–2168. https://doi.org/https://doi.org/10.1029/JB084iB05p02161

Dieterich, J.H., Kilgore, B.D., 1994. Direct observation of frictional contacts: New insights for state-dependent properties. Pure Appl. Geophys. 143, 283–302. https://doi.org/https://doi.org/10.1007/BF00874332

Faulkner, D.R., Armitage, P.J., 2013. The effect of tectonic environment on permeability development around faults and in the brittle crust. Earth Planet. Sci. Lett. 375, 71–77. https://doi.org/10.1016/j.epsl.2013.05.006

Faulkner, D.R., Sanchez-Roa, C., Boulton, C., den Hartog, S.A.M., 2018. Pore fluid pressure development in compacting fault gouge in theory, experiments, and nature. J. Geophys. Res. Solid Earth 123, 226–241. https://doi.org/10.1002/2017JB015130

Giorgetti, C., Carpenter, B.M., Collettini, C., 2015. Frictional behavior of talc-calcite mixtures. J. Geophys. Res. Solid Earth 120, 6614–6633. https://doi.org/10.1002/2015JB011970

Hillier, S., 2000. Accurate quantitative analysis of clay and other minerals in sandstones by XRD: comparison of a Rietveld and a reference intensity ratio (RIR) method and the importance of sample preparation. Clay Miner. 35, 291–302. https://doi.org/10.1180/000985500546666

Hirose, T., Hamada, Y., Tanikawa, W., Kamiya, N., Yamamoto, Y., Tsuji, T., Kinoshita, M., Heuer, B., Inagaki, F., Morono, Y., Kubo, Y., 2021. High fluid-pressure patches beneath the décollement: A potential source of slow earthquakes in the Nankai Trough off Cape Muroto. J. Geophys. Res. Solid Earth in revisio.

Ikari, M.J., Kopf, A.J., 2017. Seismic potential of weak, near-surface faults revealed at plate tectonic slip rates. Sci. Adv. 3. https://doi.org/10.1126/sciadv.1701269

Ikari, M.J., Saffer, D.M., 2011. Comparison of frictional strength and velocity dependence between fault zones in the Nankai accretionary complex. Geochemistry Geophys. Geosystems 12. https://doi.org/10.1029/2010GC003442

Ikari, M.J., Saffer, D.M., Marone, C., 2009a. Frictional and hydrologic properties of clay-rich fault gouge. J. Geophys. Res. 114. https://doi.org/10.1029/2008JB006089

Ikari, M.J., Saffer, D.M., Marone, C., 2009b. Frictional and hydrologic properties of a major splay fault system, Nankai subduction zone. Geophys. Res. Lett. 36, L20313. https://doi.org/10.1029/2009GL040009

Ikari, M.J., Saffer, D.M., Marone, C., 2007. Effect of hydration state on the frictional properties of montmorillonite-based fault gouge. J. Geophys. Res. Solid Earth 112, B06423. https://doi.org/10.1029/2006JB004748

Israelachvili, J.N., 1992. Adhesion forces between surfaces in liquids and condensable vapours. Surf. Sci. Rep. 14, 109–159. https://doi.org/10.1016/0167-5729(92)90015-4

Ito, Y., Obara, K., 2006. Dynamic deformation of the accretionary prism excites very low frequency earthquakes. Geophys. Res. Lett. 33. https://doi.org/10.1029/2005GL025270

Kimura, G., Kitamura, Y., Hashimoto, Y., Yamaguchi, A., Shibata, T., Ujiie, K., Okamoto, S., 2007. Transition of accretionary wedge structures around the up-dip limit of the seismogenic subduction zone. Earth Planet. Sci. Lett. 255, 471–484. https://doi.org/10.1016/j.epsl.2007.01.005

Kinoshita, M., Tobin, H., Ashi, J., Kimura, G., Lallemant, S., Screaton, E.J., Curewitz, D., Masago, H., Moe, K.T., Scientists, E. 314/315/316, 2009. Proceedings of the Integrated Drilling Program Expeditions 314/315/316. Integrated Ocean Drilling Program Management International, Inc. https://doi.org/doi:10.2204/iodp.proc.314315316.2009.

Kirkpatrick, J.D., Edwards, J.H., Verdecchia, A., Kluesner, J.W., Harrington, R.M., Silver, E.A., 2020. Subduction megathrust heterogeneity characterized from 3D seismic data. Nat. Geosci. 13, 369–374. https://doi.org/10.1038/s41561-020-0562-9

Kitajima, H., Hirose, T., Ikari, M., Kanagawa, K., Kimura, G., Kinoshita, M., Saffer, D., Tobin, H., Yamaguchi, A., Eguchi, N., Maeda, L., Toczko, S., Scientists, E. 358, 2020. Site C0002, in:

581 Tobin, H., Hirose, T., Ikari, M., Kanagawa, K., Kimura, G., Kinoshita, M., Kitajima, H., Saffer,
582 D., Yamaguchi, A., Eguchi, N., Maeda, L., Toczko, S., Scientists, E. 358 (Eds.), NanTroSEIZE
583 Plate Boundary Deep Riser 4: Nankai Seismogenic/Slow Slip Megathrust. Proceedings of the
584 International Ocean Discovery Program, 358, College Station, TX.
585 https://doi.org/https://doi.org/10.14379/iodp.proc.358.103.2020

586 Kodaira, S., Iidaka, T., Kato, A., Park, J.-O., Iwasaki, T., Kaneda, Y., 2004. High pore fluid pressure
587 may cause silent slip in the Nankai Trough. Science (80-. ). 304, 1295–1298.
588 https://doi.org/10.1126/science.1096535

589 Kurzawski, R.M., Niemeijer, A.R., Stipp, M., Charpentier, D., Behrmann, J.H., Spiers, C.J., 2018.
590 Frictional properties of subduction input sediments at an erosive convergent continental margin
591 and related controls on décollement slip modes: The Costa Rica Seismogenesis Project. J.
592 Geophys. Res. Solid Earth 123, 8385–8408. https://doi.org/10.1029/2017JB015398

593 Kurzawski, R.M., Stipp, M., Niemeijer, A.R., Spiers, C.J., Behrmann, J.H., 2016. Earthquake
594 nucleation in weak subducted carbonates. Nat. Geosci. 9, 717–722.
595 https://doi.org/10.1038/NGEO2774

596 Leeman, J.R., Saffer, D.M., Scuderi, M.M., Marone, C., 2016. Laboratory observations of slow
597 earthquakes and the spectrum of tectonic fault slip modes. Nat. Commun. 7.
598 https://doi.org/10.1038/ncomms11104

599 Li, Q., Tullis, T.E., Goldsby, D., Carpick, R.W., 2011. Frictional ageing from interfacial bonding and
600 the origins of rate and state friction. Nature 480, 233–236. https://doi.org/10.1038/nature10589

601 Mair, K., Marone, C., 1999. Friction of simulated fault gouge for a wide range of velocities and
602 normal stresses. J. Geophys. Res. 104, 28899–28914.
603 https://doi.org/https://doi.org/10.1029/1999JB900279

604 Marone, C., 1998. Laboratory-derived friction laws and their application to seismic faulting. Annu.
605 Rev. Earth Planet. Sci. 26, 643–696.

606 Marone, C., Raleigh, C.B., Scholz, C.H., 1990. Frictional behavior and constitutive modeling of
607 simulated fault gouge. J. Geophys. Res. 95, 7007–7025.
608 https://doi.org/https://doi.org/10.1029/JB095iB05p07007

609 Mizutani, T., Hirauchi, K., Lin, W., Sawai, M., 2017. Depth dependence of the frictional behavior of
610 montmorillonite fault gouge: Implications for seismicity along a décollement zone. Geophys.
611 Res. Lett. 44, 5383–5390. https://doi.org/10.1002/2017GL073465

612 Morrow, C.A., Moore, D.E., Lockner, D.A., 2017. Frictional strength of wet and dry montmorillonite.
613 J. Geophys. Res. Solid Earth 122, 3392–3409. https://doi.org/10.1002/2016JB013658

614 Niemeijer, A.R., Collettini, C., 2014. Frictional properties of a low-angle normal fault under in situ
615 conditions: Thermally-activated velocity weakening. Pure Appl. Geophys. 171, 2641–2664.
616 https://doi.org/10.1007/s00024-013-0759-6

617 Numelin, T., Marone, C., Kirby, E., 2007. Frictional properties of natural fault gouge from a low-
618 angle normal fault, Panamint Valley, California. Tectonics 26.
619 https://doi.org/10.1029/2005TC001916

620 Okamoto, A.S., Niemeijer, A.R., Takeshita, T., Verberne, B.A., Spiers, C.J., 2020. Frictional
621 properties of actinolite-chlorite gouge at hydrothermal conditions. Tectonophysics 779.
622 https://doi.org/10.1016/j.tecto.2020.228377

623 Okamoto, A.S., Verberne, B.A., Niemeijer, A.R., Takahashi, M., Shimizu, I., Ueda, T., Spiers, C.J.,
624 2019. Frictional properties of simulated chlorite gouge at hydrothermal conditions: Implications
625 for subduction megathrusts. J. Geophys. Res. Solid Earth 124, 4545–4565.
626 https://doi.org/10.1029/2018JB017205

627 Okazaki, K., Hirth, G., 2016. Dehydration of lawsonite could directly trigger earthquakes in
628 subducting oceanic crust. Nature 530, 81–84. https://doi.org/10.1038/nature16501

629 Okuda, H., Katayama, I., Sakuma, H., Kawai, K., 2021. Effect of normal stress on the frictional
630 behavior of brucite: application to slow earthquakes at the subduction plate interface in the

mantle wedge. Solid Earth 12, 171–186. https://doi.org/10.5194/se-12-171-2021

Park, J.-O., Tsuru, T., Kodaira, S., Cummins, P.R., Kaneda, Y., 2002. Splay fault branching along the Nankai Subduction Zone. Science (80-. ). 297, 1157–1160. https://doi.org/10.1126/science.1074111

Rabinowitz, H.S., Savage, H.M., Skarbek, R.M., Ikari, M.J., Carpenter, B.M., Collettini, C., 2018. Frictional behavior of input sediments to the Hikurangi Trench, New Zealand. Geochemistry Geophys. Geosystems 19, 2973–2990. https://doi.org/10.1029/2018GC007633

Rathbun, A.P., Marone, C., 2013. Symmetry and the critical slip distance in rate and state friction laws. J. Geophys. Res. Solid Earth 118, 3728–3741. https://doi.org/10.1002/jgrb.50224

Roesner, A., Ikari, M.J., Saffer, D.M., Stanislowski, K., Eijsink, A.M., Kopf, A.J., 2020. Friction experiments under in-situ stress reveal unexpected velocity-weakening in Nankai accretionary prism samples. Earth Planet. Sci. Lett. 538. https://doi.org/10.1016/j.epsl.2020.116180

Saffer, D.M., Frye, K.M., Marone, C., Mair, K., 2001. Laboratory results indicating complex and potentially unstable frictional behavior of smectite clay. Geophys. Res. Lett. 28, 2297–2300. https://doi.org/https://doi.org/10.1029/2001GL012869

Saffer, D.M., Marone, C., 2003. Comparison of smectite- and illite-rich gouge frictional properties: application to the updip limit of the seismogenic zone along subduction megathrusts. Earth Planet. Sci. Lett. 215, 219–235. https://doi.org/10.1016/S0012-821X(03)00424-2

Sánchez-Roa, C., Faulkner, D.R., Boulton, C., Jimenez-Millan, J., Nieto, F., 2017. How phyllosilicate mineral structure affects fault strength in Mg-rich fault systems. Geophys. Res. Lett. 44, 5457–5467. https://doi.org/10.1002/2017GL073055

Sawai, M., Niemeijer, A.R., Plümper, O., Hirose, T., Spiers, C.J., 2016. Nucleation of frictional instability caused by fluid pressurization in subducted blueschist. Geophys. Res. Lett. 43, 2543–2551. https://doi.org/10.1002/2015GL067569

Scholz, C.H., 1998. Earthquakes and friction laws. Nature 391, 37–42.

https://doi.org/https://doi.org/10.1038/34097

Scuderi, M.M., Collettini, C., 2018. Fluid injection and the mechanics of frictional stability of shale-bearing faults. J. Geophys. Res. Solid Earth 123, 8364–8384. https://doi.org/10.1029/2018JB016084

Scuderi, M.M., Collettini, C., 2016. The role of fluid pressure in induced vs. triggered seismicity: insights from rock deformation experiments on carbonates. Sci. Rep. 6. https://doi.org/10.1038/srep24852

Scuderi, M.M., Niemeijer, A.R., Collettini, C., Marone, C., 2013. Frictional properties and slip stability of active faults within carbonate-evaporite sequences: The role of dolomite and anhydrite. Earth Planet. Sci. Lett. 369–370, 220–232. https://doi.org/10.1016/j.epsl.2013.03.024

Seno, T., Stein, S., Gripp, A.E., 1993. A model for the motion of the Philippine Sea Plate consistent with NUVEL-1 and geological data. J. Geophys. Res. 98, 17941–17948. https://doi.org/https://doi.org/10.1029/93JB00782

Skarbek, R.M., Savage, H.M., 2019. RSFit3000 : A MATLAB GUI-based program for determining rate and state frictional parameters from experimental data. Geosphere 15, 1665–1676. https://doi.org/https://doi.org/10.1130/GES02122.1

Smith, S.A.F., Faulkner, D.R., 2010. Laboratory measurements of the frictional properties of the Zuccale low-angle normal fault, Elba Island, Italy. J. Geophys. Res. 115, B02407. https://doi.org/10.1029/2008JB006274

Sugioka, H., Okamoto, T., Nakamura, T., Ishihara, Y., Ito, A., Obana, K., Kinoshita, M., Nakahigashi, K., Shinohara, M., Fukao, Y., 2012. Tsunamigenic potential of the shallow subduction plate boundary inferred from slow seismic slip. Nat. Geosci. 5, 414–418. https://doi.org/10.1038/ngeo1466

Terzaghi, K., 1943. Theoretical soil mechanics. New York: Wiley, 1943.

Thom, C.A., Carpick, R.W., Goldsby, D.L., 2018. Constraints on the physical mechanism of frictional

681 aging from nanoindentation. Geophys. Res. Lett. 45, 13306–13311.
682 https://doi.org/10.1029/2018GL080561

683 Tobin, H., Hirose, T., Ikari, M., Kanagawa, K., Kimura, G., Kinoshita, M., Kitajima, H., Saffer, D.,
684 Yamaguchi, A., Eguchi, N., Maeda, L., Toczko, S., Scientists, E. 358, 2020. Expedition 358
685 summary, in: Tobin, H., Hirose, T., Ikari, M., Kanagawa, K., Kimura, G., Kinoshita, M.,
686 Kitajima, H., Saffer, D., Yamaguchi, A., Eguchi, N., Maeda, L., Toczko, S., Scientists, E. 358
687 (Eds.), NanTroSEIZE Plate Boundary Deep Riser 4: Nankai Seismogenic/Slow Slip Megathrust.
688 Proceedings of the International Ocean Discovery Program, 358, College Station, TX.
689 https://doi.org/https://doi.org/10.14379/iodp.proc.358.101.2020

690 Tobin, H.J., Kinoshita, M., 2006. NanTroSEIZE: The IODP Nankai Trough Seismogenic Zone
691 Experiment. Sci. Drill. 2, 23–27. https://doi.org/10.2204/iodp.sd.2.06.2006

692 Tobin, H.J., Saffer, D.M., 2009. Elevated fluid pressure and extreme mechanical weakness of a plate
693 boundary thrust, Nankai Trough subduction zone. Geology 37, 679–682.
694 https://doi.org/10.1130/G25752A.1

695 Tsutsumi, A., Fabbri, O., Karpoff, A.M., Ujiie, K., Tsujimoto, A., 2011. Friction velocity dependence
696 of clay-rich fault material along a megasplay fault in the Nankai subduction zone at intermediate
697 to high velocities. Geophys. Res. Lett. 38. https://doi.org/10.1029/2011GL049314

698 Ujiie, K., Tsutsumi, A., 2010. High-velocity frictional properties of clay-rich fault gouge in a
699 megasplay fault zone, Nankai subduction zone. Geophys. Res. Lett. 37.
700 https://doi.org/10.1029/2010GL046002

701 Warren-Smith, E., Fry, B., Wallace, L., Chon, E., Henrys, S., Sheehan, A., Mochizuki, K., Schwartz,
702 S., Webb, S., Lebedev, S., 2019. Episodic stress and fluid pressure cycling in subducting oceanic
703 crust during slow slip. Nat. Geosci. 12, 475–481. https://doi.org/10.1038/s41561-019-0367-x

704 Xing, T., Zhu, W., French, M., Belzer, B., 2019. Stabilizing effect of high pore fluid pressure on slip
705 behaviors of gouge-bearing faults. J. Geophys. Res. Solid Earth 124, 9526–9545.

706 https://doi.org/10.1029/2019JB018002

707